Nano Research

Open Access

Research Article

Hierarchical hollow microspheres assembled from carbon nanosheets integrated with molybdenum carbide nanoparticles for boosting microwave absorption properties

Zongsheng Chen[1,2], Yahui Wang[1,2] ✉, Yi Liu[1,2], Zhigang Li[1,2], Xiangyin Lv[1,2], Liping Liu[1,2], Yajing Chang[1,2], Jiaming Shi[1,2], and Xiao Zhang[3] ✉

[1] *State Key Laboratory of Pulsed Power Laser Technology, School of Electronic Engineering, National University of Defense Technology, Hefei 230037, China*
[2] *Anhui Provincial Laboratory of Advanced Laser Technology, School of Electronic Engineering, National University of Defense Technology, Hefei 230037, China*
[3] *Centre for Environmental and Energy Nanomaterials, Anhui Key Laboratory of Nanomaterials and Nanotechnology, CAS Centre for Excellence in Nanoscience, Institute of Solid State Physics, Hefei Institutes of Physical Science, Chinese Academy of Sciences, Hefei 230031, China*

Cite this article: *Nano Research*, **2025**, *18*, 94907034. https://doi.org/10.26599/NR.2025.94907034

ABSTRACT: Hierarchical hollow structure has demonstrated potential for enhancing electromagnetic (EM) attenuation and improving impedance matching, garnering significant attention for researching. Herein, we have successfully implemented compositional and structural engineering to fabricate hollow Mo_2C/C microspheres with controllable composition by coupling interaction between dopamine hydrochloride and ammonium molybdate. With the synergistic effect of composition and hollow structure, the strongest reflection loss intensity and broadest effective absorption of the optimized sample reach –70.2 dB and 6.2 GHz, respectively. The formation of hollow heterogeneous structures not only favors impedance matching feature, but also generates considerable contribution to EM attenuation capacity. Furthermore, radar cross-section simulation data indicate that hollow Mo_2C/C microspheres with compositional optimization and heterogeneous structures have broad prospects for practical applications.

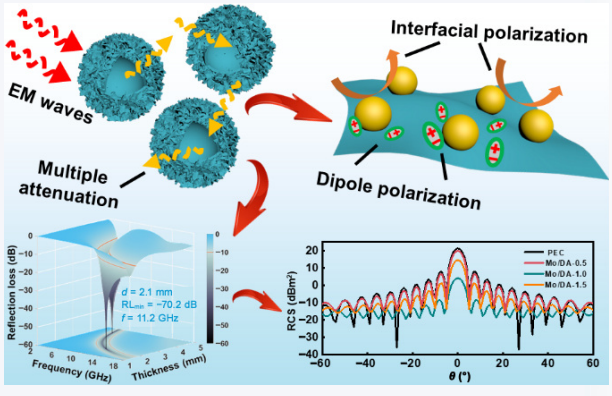

KEYWORDS: electromagnetic absorption, Mo_2C/C, microwave absorption, hollow structure

1 Introduction

The extensive application of advanced fifth-generation (5G) electronic equipment has increased the convenience of social production and daily life, while the accompanying electromagnetic (EM) radiation and EM leakage seriously threatened human health and industrial production [1–3]. In recent years, EM absorption materials have demonstrated satisfactory contribution in reducing EM radiation and preventing EM leakage [4]. It is more sights focused on the preparation of carbon-based magnetic EM absorption materials because of their dual attenuation mechanism with magnetic loss and dielectric loss [5–7]. Despite the fact that many carbon-based magnetic composites have achieved commendable progress in reflection loss (RL) and effective absorption bandwidth (EAB), the existence of magnetic nanoparticles does not produce powerful magnetic loss characteristics, and their EM energy dissipation mainly contributed from dielectric loss [8]. Based on these studies, researchers have gradually hammered at new carbon-based dielectric loss composites [9–11]. They attempted to replace magnetic components with dielectric components for enhancing EM absorption property, and meanwhile avoiding the drawback of high density and easy oxidation in magnetic particles.

Among of various dielectric components, molybdenum carbide

Received: August 1, 2024; **Revised:** September 10, 2024
Accepted: September 13, 2024

✉Address correspondence to Yahui Wang, wangyahui22@nudt.edu.cn; Xiao Zhang, zhangxiao@issp.ac.cn

(Mo_2C) is emerging as potential EM absorption materials because of their good conductivity, thermal stability, and corrosion resistance [12–16]. Recent applications of Mo_2C have further enhanced the EM absorption of carbon-based composites. For example, Dai et al. fabricated porous-carbon-based Mo_2C nanocomposite as their pioneering investigation into its EM absorption performance, and they found that its effective absorption overcomes the disadvantage that carbonaceous composites always occur in the high-frequency region [12]. Yang et al. manufactured a series of Mo_2C/NC@MXene composites by carbonizing the precursor created through wrapping MXene nanosheets on the MoO_3/PDA flower-like particle, and the multiple reflection in the lamella structure contributed to the enhancement EM absorption property [13]. Our group recently also synthesized various Mo_2C/C composites including polyhedral Mo_2C/C, core–shell Mo_2C@C, and Mo_2C/C/rGO aerogel, and we found that the introduction of small-sized Mo_2C could indeed modulate the impedance matching and induce affluent interfacial polarization in carbon host [14–16]. However, all these composites suffer from insufficient nanostructure and only blending of different components, which will limit the further improvement of EM absorption performance. In addition to the inherent attenuation properties, the internal structure of composites also affects their EM absorption properties. Some diligent designed microstructures, like core–shell, hollow, and multilayer, have been widely adopted to intensify the EM wastage intensity through providing multiple reflection and scatter [17–19]. Particularly, hollow structure has been emerging as a type of supporting substrates for promoting EM absorption performance because of the low density and affluent specific surface area. Besides, multiple attenuation effects will be induced generation at the interior cavity, extending the propagation path of incident EM waves, and the internal air makes their impedance closer to that of free space, which are both conducive to the consumption of incident EM wave [19]. To date, some hollow-structure Mo_2C/C composites have been developed to enhance EM absorption [20–22]. For example, Zhao et al. prepared different hollow structure and different crystalline phases of Mo_2C/C composites, and they found that hollow structure can optimize impedance matching. Meanwhile, it exhibited appreciable EM absorption property with the minimum RL of –50.55 dB and a EAB of 5.36 GHz, which is superior to that of some Mo_2C/C composites lacking nanostructure [21]. However, the existing synthesis strategy of hollow Mo_2C/C composites usually involves high-temperature hydrothermal process or etching treatments, which will not be conducive to the promotion of Mo_2C/C composites in practical application. Therefore, the fabrication of hollow Mo_2C/C composites in a simple method for developing EM absorption performance remains a considerable challenge.

Herein, a hierarchical hollow microsphere composed of Mo_2C nanoparticles decorated carbon nanosheets has been synthesized by converting the precursor obtained by coupling interaction between dopamine hydrochloride and ammonium molybdate ($(NH_4)_6Mo_7O_{24}{\cdot}4H_2O$, AM) under high temperature. The carbonaceous matrix can serve as a restriction to impede the aggregation of Mo_2C nanoparticle, and the uniformly dispersed tiny Mo_2C particles also achieve the maximum heterogeneous interface for providing affluent interfacial polarization loss. Meanwhile, the hierarchical nanosheets and internal hollow structure will prolong the propagation path of incident EM waves and induce multiple attenuation effects. Benefitting from the well-organized component and hierarchical hollow structure, the resultant Mo_2C/C microsphere gives gratifying EM absorption performance with a strong RL of –70.2 dB with a thickness of 2.1 mm and EAB of 6.2 GHz at a corresponding thickness of 1.7 mm. The facile and green synthetic process and desirable EM absorption property of hollow Mo_2C/C microsphere precipitate them expected as anticipant EM absorption materials for practical application.

2 Experimental section

2.1 Materials

Dopamine hydrochloride and ammonium molybdate were purchased from Aladdin Technology Co. Ltd., Shanghai, China. Absolute ethanol and ammonium hydroxide solution ($NH_3{\cdot}H_2O$, 25%–28%) were purchased from Sinopharm Chemical Reagent Co., Ltd., Shanghai, China. The above reagents were all analytical grade and were used without any other treatment. Deionized water was prepared using the standard ultrapure water system in our laboratory.

2.2 Synthesis of hierarchical hollow Mo_2C/C microsphere

In a typical synthesis, a certain amount of AM was dissolved in 30 mL of deionized water and vigorously stirred for 10 min at room temperature until completely dissolved. Then, 303 mg of dopamine hydrochloride was added to the solution, resulting in a reddish-brown solution. To this mixture, 60 mL of absolute ethanol and 0.4 mL of $NH_3{\cdot}H_2O$ were added subsequently to form an orange-red suspension under stirring. The suspension was stirred continuously for an additional 3 h and then collected through centrifugation. The obtained solid powder was washed several times with deionized water and absolute ethanol, followed by drying at 70 °C for 8 h. Finally, the as-prepared precursors were transferred to a tubular furnace and pyrolyzed at 700 °C under an Ar atmosphere for 2 h, with a heating rate of 5 °C/min. For convenience, the molar ratios of AM/dopamine hydrochloride were 0.5:1, 1:1, and 1.5:1, and the final composites were labeled as Mo/DA-0.5, Mo/DA-1.0, and Mo/DA-1.5, respectively.

2.3 Characterization

An X'PERT PRO MPD X-ray diffractometer was employed to record X-ray diffraction (XRD) data with a Cu Kα radiation source (40.0 kV, 40.0 mA). Raman spectra were detected on a confocal Raman spectroscopic system (Renishaw, In Via) using a 532 nm laser. The HELIOS NanoLab 600i (FEI) was employed to obtain scanning electron microscopy (SEM) images. Transmission electron microscopy (TEM) images and high-resolution TEM (HRTEM) images were recorded on a Tecnai F20 operating at an accelerating voltage of 200 kV. The thermogravimetric (TG) analysis was determined on an SDT Q600 TGA (TA Instruments) in the temperature range of room temperature to 700 °C at a heating rate of 10 °C/min under the air atmosphere. An Ceyear AV3672C vector network analyzer (Ceyear, China) was applied to determine the relative permeability (μ_r) and permittivity (ε_r) in the frequency range of 2.0–18.0 GHz for the calculation of RL. A sample containing 40 wt.% of the obtained composites was pressed into a ring with an outer diameter of 7.0 mm, an inner diameter of 3.0 mm, and a thickness of 2.0 mm for microwave measurement in which paraffin wax was used as a binder.

3 Results and discussion

The preparation process of heterogeneous hollow Mo_2C/C

nanospheres is depicted in Fig. 1. Initially, dopamine hydrochloride and ammonium molybdate reacted in an aqueous solution, leading to the formation of a Mo-dopamine complex. Subsequently, the addition of ethanol induced the generation of nanobubbles and precipitates. These precipitates underwent self-assembly at the interface between the gas and liquid phases, resulting in the formation of a Pickering emulsion [23]. Then, ammonia was introduced, triggering the polymerization of the Mo-dopamine complex, and forming a sturdy shell around the nanobubbles. Subsequent cross-linking further stabilized the hollow structure. Finally, the hollow Mo-polydopamine composite nanospheres were subjected to carbonization at 700 °C for 2 h, resulting in the formation of heterogeneous hollow Mo_2C/C composite nanospheres. These nanospheres were composed of ultrathin carbon nanosheets and ultrafine Mo_2C nanoparticles.

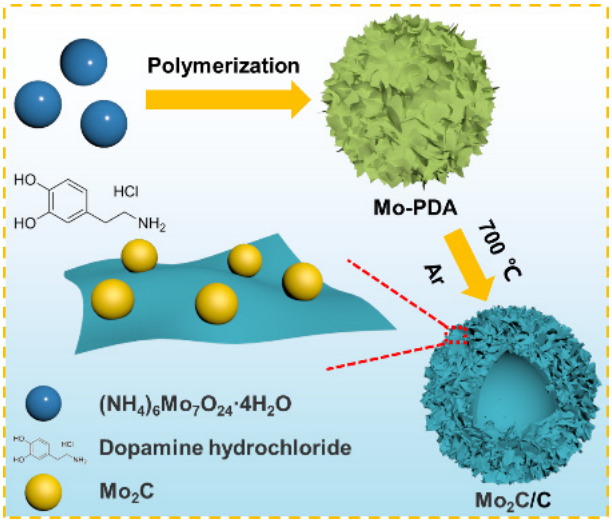

Figure 1 The preparation process of hierarchical hollow Mo_2C/C nanospheres.

The samples obtained in the study were analyzed in terms of their morphology and structure. It is observed that samples with varying Mo_2C contents exhibited a consistent spherical morphology. Figure 2(a) displays the SEM image of the composite obtained with a molar ratio of molybdenum to dopamine (Mo/DA) of 1:1 in the precursor. The image clearly demonstrates that the Mo_2C/C composite possesses a regular spherical shape with uniform size and homogeneous dispersion, featuring an average sphere size of 300 nm. TEM images of Mo/DA-0.5, Mo/DA-1.0, and Mo/DA-1.5 are shown in Figs. 2(b)–2(d), respectively. These images reveal that all three samples exhibit distinct hollow hierarchical structures. Notably, the magnified TEM image (Fig. 2(e)) illustrates that the spherical surface is composed of numerous interlaced nanosheets. This arrangement of nanosheets enhances the specific surface area of the composite material, providing abundant heterogeneous interfaces and facilitating electromagnetic polarization loss. Additionally, higher-resolution TEM images (Figs. 2(f)–2(h)) demonstrate the uniform dispersion of black Mo_2C nanoparticles within the Mo_2C/C composite materials of different proportions. As the Mo/DA ratio increases, the quantity of Mo_2C particles gradually rises, indicating the ability to obtain Mo_2C/C composite materials with adjustable compositions by tailoring the molybdenum salt content in the precursor. Moreover, the uniformly dispersed tiny Mo_2C particles within the carbon matrix contribute to the abundance of heterogeneous interfaces, thereby enhancing the interface polarization loss of the material. High-resolution TEM analysis reveals that the size of the Mo_2C particles is smaller than 10 nm, and the observed lattice fringes correspond well with the (101) crystal plane of the cubic-phase Mo_2C [16, 24].

As shown in Fig. 3(a), Mo/DA-0.5, Mo/DA-1.0, and Mo/DA-1.5 display distinct characteristic diffraction peaks at 2θ = 37.8°, 43.7°, 63.4°, and 75.8°, which correspond to the (111), (200), (220), and (311) crystal planes of cubic Mo_2C, respectively [13, 15]. The consistent characteristic diffraction peaks across these samples indicate the successful attainment of well-crystallized Mo_2C. Based on those characteristic diffraction peaks, it is evident that these composites obtained exhibit broad peak widths. This phenomenon is consistent with the Scherrer equation, which establishes an inverse relationship between the XRD peak width and the crystal grain size [25]. A broader peak width indicates a smaller crystal grain size. Consequently, the smaller grain size of the obtained Mo_2C aligns with the results depicted in the TEM images. As widely recognized, the conductivity of carbon material is critical for the EM waves attenuation [26–29]. In the case of carbon materials, graphitization degree significantly impacts electrical conductivity. According to free electron theory ($\varepsilon_r'' \approx \sigma/\omega\varepsilon_0$, σ is conductivity) [29], a higher conductivity corresponds to a stronger ability to dissipate EM energy. Actually, the graphitization degree in carbon composite demonstrates a direct correlation with their EM attenuation [10, 30]. Hence, Raman spectroscopy is employed to accurately assess the level of graphitization in Mo_2C/C composite. According to Fig. 3(b), Mo/DA-0.5, Mo/DA-1.0, and Mo/DA-1.5 all exhibit two distinct Raman shift peaks at approximately 1350 and 1590 cm^{-1} [31, 32]. These peaks can be attributed to the D band and G band of carbon, respectively. The D band indicates the degree of disorder, while the G band represents the level of graphitization [7]. The graphitization degree is commonly expressed by the ratio of I_D/I_G. For graphited carbon, a smaller I_D/I_G value indicates a higher level of graphitization [24, 33]. Conversely, in the case of amorphous carbon, larger I_D/I_G value suggests a high graphitization degree. This phenomenon can be explained by the formation of carbon nanocrystals during the transformation process from amorphous carbon to graphitic carbon. The increasing I_D/I_G value in the Raman spectrum serves as an indicator of this transition. The carbon layer in our case is determined to be composed of amorphous carbon. Consequently, an elevated I_D/I_G value indicates a higher level of graphitization. In our case, the I_D/I_G values of Mo/DA-0.5, Mo/DA-1.0, and Mo/DA-1.5 decrease from 0.90 to 0.88. This trend is depicted in Fig. 3(b), which demonstrates a faint decrease in I_D/I_G value as the Mo/DA ratio increases. It is implied that the incorporation of Mo_2C nanoparticles results in a negative effect on the graphitization degree of carbon matrix. This effect primarily stems from the increased presence of defects sites caused by the inclusion of Mo_2C nanoparticles.

TG analysis can be employed to obtain the relative percentage content of Mo_2C in those Mo_2C/C composites. It can be seen that three samples all demonstrate consistent variation curves in Fig. 3(c). These curves exhibit mainly three stages of weight variation. The first stage is from 25–400 °C, which is primarily the evaporation of adsorbed moisture [14, 34]. The second stage mainly involves the oxidation of carbon and Mo_2C in Mo_2C/C composites (400–750 °C). The third stage is the stable stage after the oxidation of Mo_2C/C (750–800 °C) [22, 35]. Based on the oxidation chemical equation: $Mo_2C + 4O_2 \rightarrow 2MoO_3 + CO_2$ [15, 16, 24], the relative content of Mo_2C in the Mo/DA-0.5, Mo/DA-1.0, and Mo/DA-1.5 composites can be obtained from the percentage of remaining substances after oxidation, which is approximately 38.3%, 43.2%,

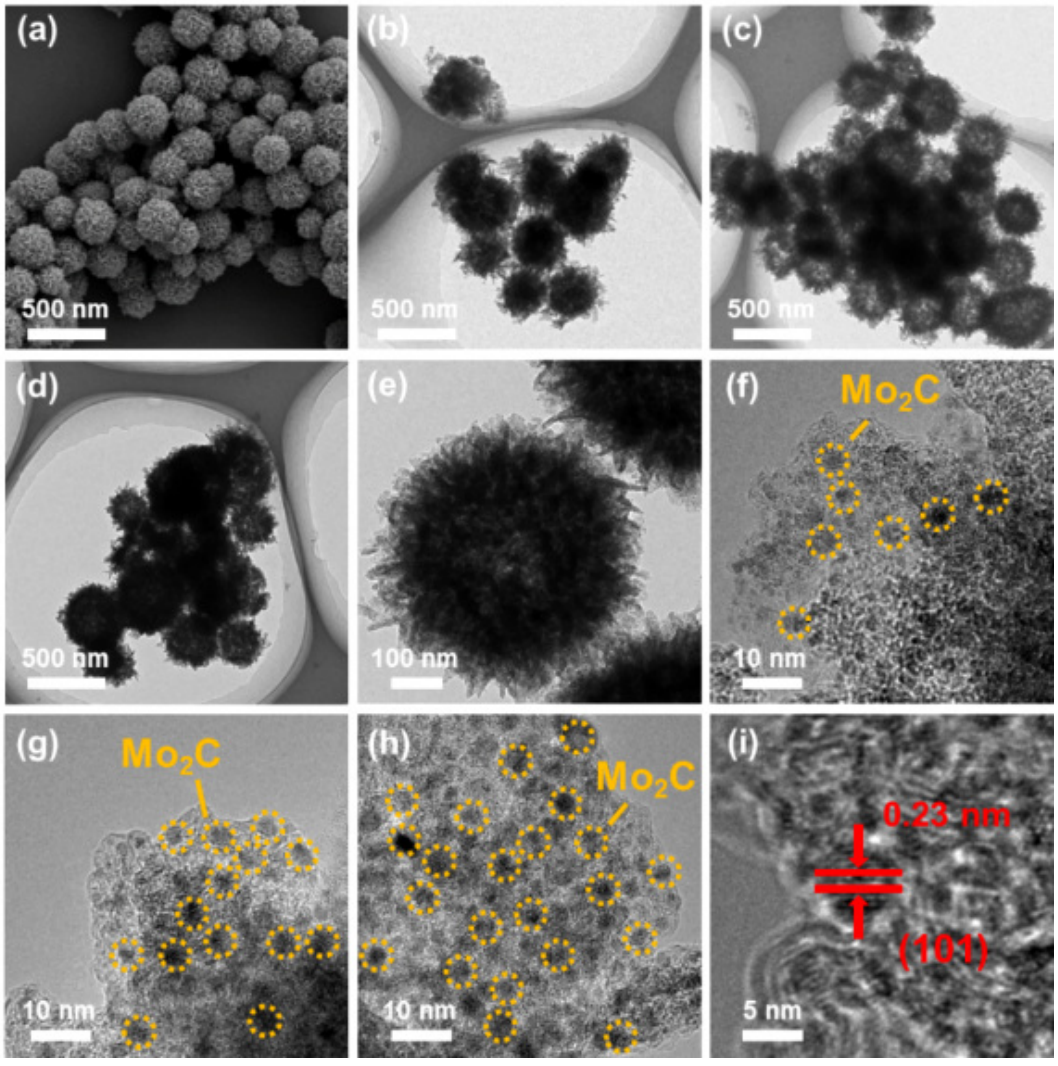

Figure 2 (a) SEM image of precursor with Mo/DA = 1:1. TEM images of (b) and (f) Mo/DA-0.5, (c), (e), and (g) Mo/DA-1.0, and (d) and (h) Mo/DA-1.5. (i) HRTEM image of Mo/DA-1.0.

and 46.1%, respectively. This statement implies that the composition of Mo_2C/C composites can be tailored by modifying the AM content in the precursor. The XPS survey analysis in Fig. S1 in the Electronic Supplementary Material (ESM) clearly identifies distinct signals corresponding to the elements of C, Mo, and N in the Mo_2C/C composites, providing additional evidence of their chemical composition. The research findings reveal that the C 1s spectrum exhibits four distinct peaks, illustrated in Fig. 3(d), attributed to specific bonds: C=O (289.2 eV), C=N (286.1 eV), C–C (285.3 eV), and C–Mo (284.3 eV) [36–38]. Analysis of the Mo 3d spectrum (Fig. 3(e)) identifies six peaks corresponding to Mo^{2+} (228.9 and 231.8 eV), Mo^{4+} (229.6 and 233.1 eV), and Mo^{6+} (232.2 and 235.9 eV) [39–41]. Although there is an overlap between the Mo 3p and N 1s in XPS spectra, the N 1s becomes clearly distinguishable when these spectra are appropriately amplified (Fig. 3(e)). Graphite-N, pyridine-N, and pyrrole-N represent the three primary configurations of N 1s in these composites in Fig. 3(f) [42, 43]. The observed increase in the relative intensity of Mo 3p from Mo/DA-0.5 to Mo/DA-0.5 provides further evidence of the adjustable Mo_2C content within these composites. It is widely believed that N-doped in the carbon framework can act as defect sites, influencing EM absorption through dipole polarization loss.

RL intensity and EAB are two critical indicators for evaluating the microwave absorption characteristics EM absorption materials [44–46]. RL represents the attenuation ability of EM absorption materials at a specific frequency, while EAB describes the frequency range over which the RL is below −10 dB, where −10 dB is considered as 90% EM energy consumption [47–49]. The RL value can be calculated using the following Eqs. (1) and (2) [50–52]

$$RL = -20 \log \left| \frac{z_{in} - 1}{z_{in} + 1} \right| \quad (1)$$

$$Z_{in} = \sqrt{\frac{\mu_r}{\varepsilon_r}} \tanh \left[j \left(\frac{2\pi}{c} \right) fd \sqrt{\mu_r \varepsilon_r} \right] \quad (2)$$

where Z_{in} is the input impedance of absorbent, c and f are the velocity and frequency of EM waves in free space, and d is the absorber thickness. Figures 4(a)–4(c) display the three-dimensional (3D) RL maps of different Mo_2C/C composites, with the two variables of frequency (2.0–18.0 GHz) and thickness (1.0–5.0 mm). One can see that while all samples exhibit EM loss characteristics, there are notable differences among them. As shown in Fig. 4(a), at a thickness of 2.1 mm, the minimum RL (RL_{min}) value of Mo/DA-

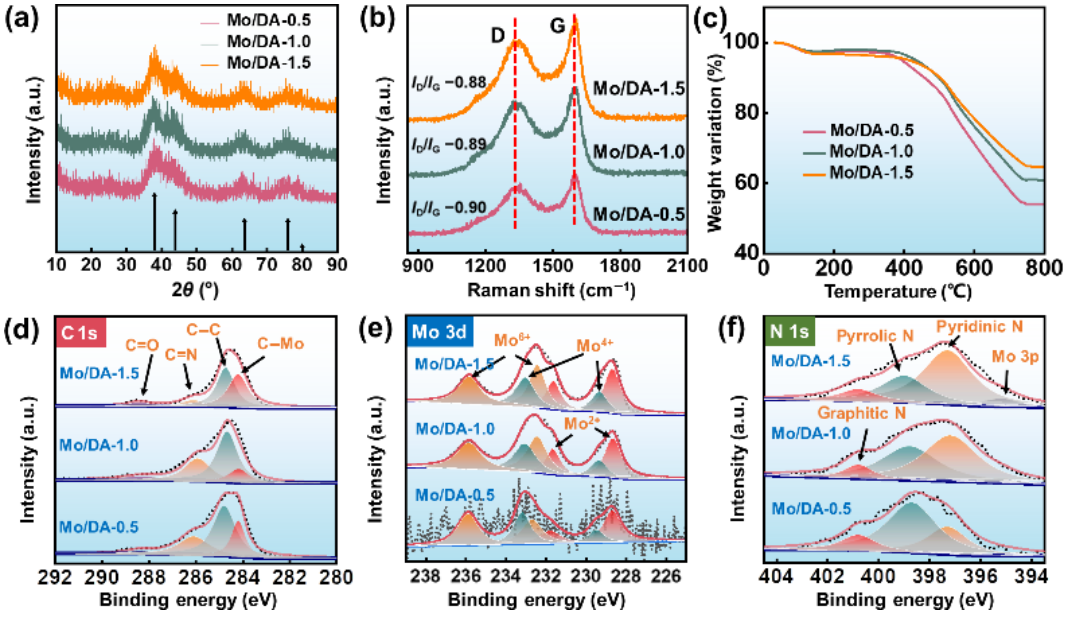

Figure 3 (a) XRD patterns, (b) Raman spectra, and (c) TG curves. XPS spectra of (d) C 1s, (e) Mo 3d, (f) N 1s of Mo/DA-0.5, Mo/DA-1.0, and Mo/DA-1.5.

0.5 is only −17.2 dB, corresponding to a frequency of 8.8 GHz. With the increase in Mo_2C content, Mo/DA-1.0 reaches a RL_{min} value of −70.2 dB at a thickness of 2.1 mm, corresponding to the frequency of 11.2 GHz (Fig. 4(b)). When the Mo_2C content is further increased, the RL_{min} value of Mo/DA-1.5 decreases to −35.6 dB, corresponding to a thickness of 1.6 mm and a frequency of 18 GHz (Fig. 4(c)). In addition to RL_{min}, the maximum EAB of Mo/DA-0.5, Mo/DA-1.0, and Mo/DA-1.5 also varies. Figures 4(c)–4(e) show the projected two-dimensional (2D) RL maps, showing that the maximum EAB of these three samples follows a similar pattern to the RL_{min} value. Specifically, Mo/DA-0.5 reaches an EAB of 2.9 GHz at a thickness of 1.4 mm, Mo/DA-1.0 exhibits the maximum EAB of 6.2 GHz, and the maximum EAB of Mo/DA-1.5 is only 3.1 GHz at a thickness of 1.9 mm. When we comprehensive comparison of the properties of Mo/DA-0.5, Mo/DA-1.0, and Mo/DA-1.5 (Fig. 4(g)) indicate that Mo/DA-1.0 is the optimized candidate due to its strong absorption and wide response bandwidth. Comparing the properties of Mo_2C/C composites reported in recent years further verifies the superior EM absorption properties of Mo/DA-1.0 (Figs. 4(h) and 4(i)) [12, 13, 15, 16, 24, 53–55]. The dominant positions of both the RL_{min} and EAB for Mo/DA-1.0 underscore the importance of composition regulation and heterogeneous hollow engineering.

Furthermore, as shown in Figs. 4(j)–4(l), the thicknesses corresponding to RL_{min} values less than −10 dB for Mo/DA-0.5, Mo/DA-1.0, and Mo/DA-1.5 conform to the quarter-wavelength model, that is Eq. (3) [56, 57],

$$d_m = \frac{n\lambda}{4} = \frac{nc}{4f_m\sqrt{|\mu_r||\varepsilon_r|}} (n = 1, 3, 5.....) \quad (3)$$

where d_m denotes thickness, f_m is the frequency corresponding to RL_{min}, and λ, c, $|\mu_r|$, and $|\varepsilon_r|$ represent wavelength, speed of light, permeability, and permittivity, respectively. When the thickness of the EM absorption material is an odd multiple of a quarter wavelength, a half-cycle phase shift occurs between the incident and reflected EM waves, leading to continuous attenuation of the reflected wave. The theoretical values, calculated using the Eq. (3), are depicted by pink line segments, while the experimental data are shown as purple symbols. The results indicate that all three samples align well with the quarter-wavelength model.

According to transmission line theory, the EM absorption characteristics are primarily determined by relative complex permittivity and complex permeability [58, 59]. Therefore, within the frequency range of 2.0–18.0 GHz, an analysis of relevant EM parameters was conducted to explore the inherent reasons for the differences in the microwave absorption performance of Mo_2C/C composites. As these Mo_2C/C composites do not contain any magnetic components, the real and imaginary parts of relative complex permeability are nearly constant, approaching 1 and 0, respectively (Fig. S2 in the ESM). This indicates that these composites cannot dissipate electromagnetic energy through magnetic losses. Figures 5(a) and 5(b) illustrate the real part (ε_r') and imaginary part (ε_r'') of the permittivity for various Mo_2C/C composites, and these dielectric constants demonstrate noticeable frequency-dependent characteristics. Among the three samples, Mo/DA-0.5 exhibits the highest values of ε_r' and ε_r'', with ε_r' decreasing from 17.9 at 2.0 GHz to 12.6 at 18.0 GHz, and ε_r'' decreasing from 9.0 at 2.0 GHz to 7.0 at 18.0 GHz. As the Mo_2C content increases, both Mo/DA-1.0 and Mo/DA-1.5 display decreasing values of ε_r' and ε_r''. Specifically, for Mo/DA-1.5, ε_r' decreases from 8.9 at 2.0 GHz to 7.1 at 18.0 GHz, and ε_r'' decreases from 1.7 at 2.0 GHz to 2.1 at 18.0 GHz. There is abundant literature evidence indicating a positive correlation between conductivity and ε_r, and higher ε_r leads to increased attenuation of EM energy [56–60]. In our case, an increase in the content of Mo_2C results in a gradual decrease in the dielectric constant, consistent with findings from Raman spectra. These results suggest that higher Mo_2C content diminishes the dielectric loss capability of composites. Figure 5(c) shows the values of tanδ, which intuitively represents the dielectric loss capability of the composite [57]. It can be observed that Mo/DA-0.5 exhibits the highest dielectric loss capability in Fig. 5(c), while the tanδ value of Mo/DA-1.5 is even less than 0.2, indicating a weaker dielectric loss capability.

For an extended period, it has been believed that dielectric loss stems from both conductivity loss and polarization loss. Conductivity loss correlates strongly with the movement of free charge carriers in EM field, whereas polarization loss arises from

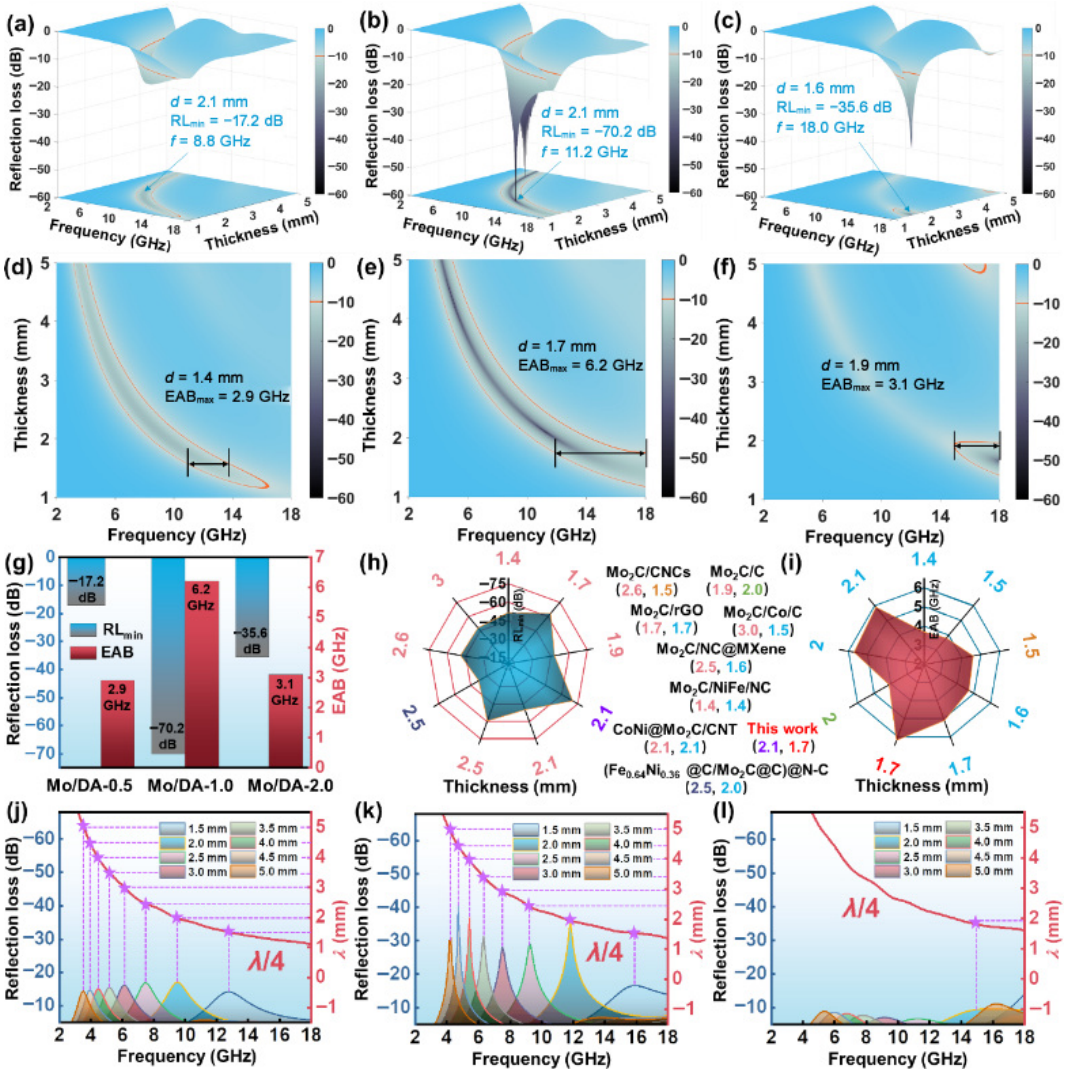

Figure 4 (a)–(c) The 3D RL maps, (d)–(f) 2D RL maps, (g) RL_{min} and EAB of Mo/DA-0.5, Mo/DA-1.0; (h) and (i) Mo_2C/C composites reported in recent years; quarter wavelength model of (j) Mo/DA-0.5, (k) Mo/DA-1.0, and (l) Mo/DA-1.5, respectively.

the relaxation movement of charged particles [51–54]. In terms of polarization loss, interfacial and dipolar polarization losses are the primary contributors to EM energy attenuation. This is because the flexibility and rapid response of electronic and ionic polarization cannot effectively convert EM energy [55, 56]. Interfacial polarization arises from the asymmetrical accumulation of space charges at heterogeneous interfaces, which can generate an electric dipole moment and result in increased energy consumption. Additionally, dipole polarization is induced by the hysteretic reorientation of dipoles in response to an applied electric field [16]. The polarization process can be demonstrated by analyzing the semicircle in the ε_r' vs. ε_r'' plot according to Debye theory, represented by the following Eq. (4) [55–57]

$$\left(\varepsilon_r' - \frac{\varepsilon_s + \varepsilon_\infty}{2}\right)^2 + \varepsilon_r''^2 = \left(\frac{\varepsilon_s - \varepsilon_\infty}{2}\right)^2 \quad (4)$$

where ε_s is the static dielectric and ε_∞ is dielectric constant at infinite frequency. Debye theory indicates that each polarization process will correspond to a semicircle, which is known as Cole–Cole semicircle [35]. The ε_r' vs. ε_r'' curves of Mo/DA-0.5, Mo/DA-1.0, and Mo/DA-1.5 have been plotted in Figs. S3(a)–S3(c) in the ESM according to Eq. (4). One can see that three samples give distinct semicircles, and they exhibit different-slope line at the region of high ε_r' values. This indicates that, in addition to polarization loss, there is also contribution from conductivity loss. When the contribution of conductivity loss to dielectric loss is insufficient, the Cole–Cole semicircle will dominate the whole curve with severe distortions [22]. As shown in Figs. S3(a) and S3(b) in the ESM, Mo/DA-0.5 and Mo/DA-1.0 exhibit visible straight lines at the end of the Cole–Cole semicircle, implying conductivity loss will give a prominent contribution to dielectric loss. With the increase of Mo_2C nanoparticles, the straight line of Mo/DA-1.0 displays feeble, which indicates polarization loss dominating the contribution for dielectric loss. To further illustrate the contributions of polarization loss and conductivity loss, we quantified the contributions of conductivity loss (ε_c'') and polarization loss (ε_p'') in different composites based on the Debye relaxation model fitted using the least squares method [50–52]. It becomes evident that with increasing frequency, the contribution of ε_c'' gradually decreases in Fig. 5(d). Concurrently, the intensity of ε_c'' is highly consistent with the $\tan\delta_e$ of various Mo_2C/C composites. Unlike conductivity loss, the contribution of polarization loss in these composites increases progressively from 2.0 to 18.0 GHz in Fig. 5(e). These results

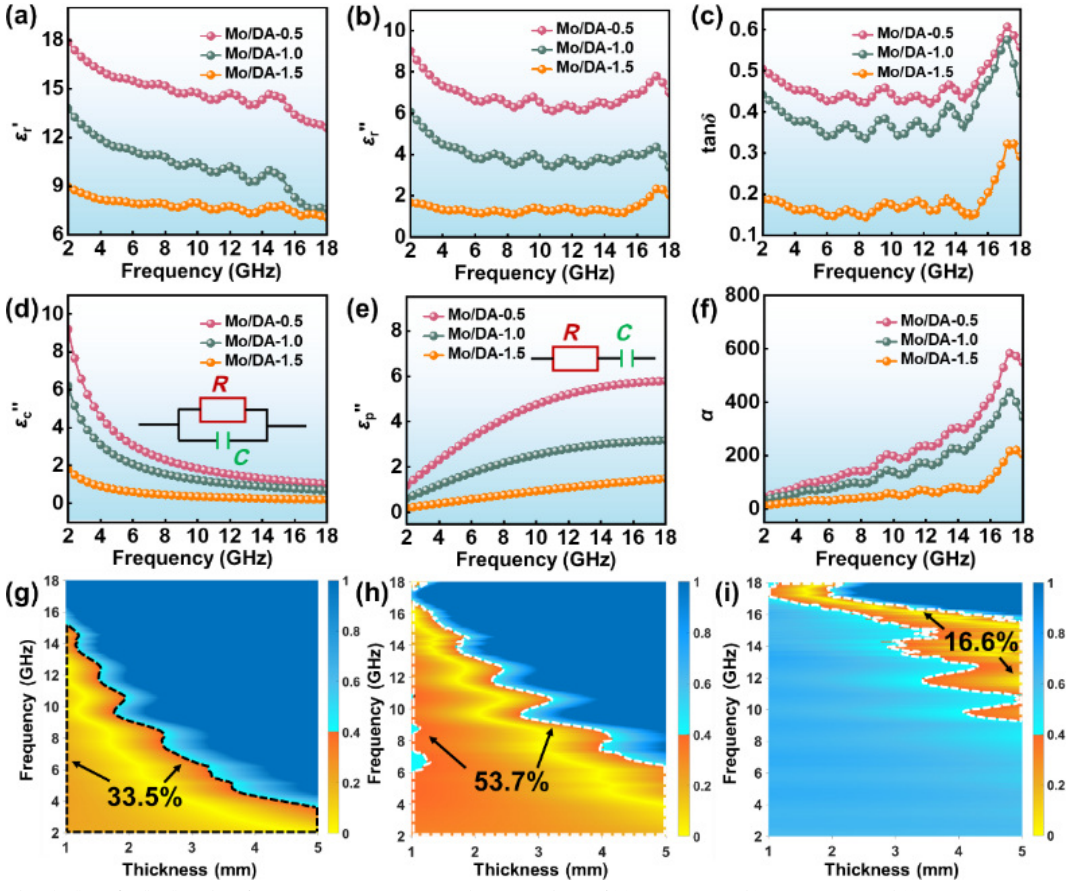

Figure 5 (a)–(f) The ε_r', ε_r'', tanδ, ε_c'', ε_p'', and α of Mo_2C/C composites. Impedance matching of (g) Mo/DA-0.5, (h) Mo/DA-1.0, and (i) Mo/DA-1.5, respectively.

indicate that the substantial dielectric loss in Mo_2C/C is primarily due to the combined effects of conductivity loss and polarization loss.

Attenuation constant (α) describes the amplitude decay of EM waves in a transmission medium [61]. Recent research frequently employs it to characterize the absorption capability, as depicted in Eq. (5) [8, 22]

$$\alpha = \frac{\sqrt{2}\pi f}{c}\sqrt{(\mu_r''\varepsilon_r'' - \mu_r'\varepsilon_r') + \sqrt{(\mu_r''\varepsilon_r'' - \mu_r'\varepsilon_r')^2 + (\mu_r'\varepsilon_r'' + \mu_r''\varepsilon_r')^2}} \quad (5)$$

According to Eq. (5), curves illustrating the variation of α values with frequency for different Mo_2C/C composites were plotted. Figure 5(f) shows that the α values for all composites increase from 2.0 to 18.0 GHz. Interestingly, the ordering of α values among the three samples correlates with their tanδ values, suggesting that dielectric loss predominantly contributes to EM attenuation. Despite Mo/DA-0.5 exhibiting the highest complex permittivity, tanδ, and α values among these composites (Figs. 5(a)–5(c) and 5(f)), it does not achieve optimal microwave absorption performance (Figs. 4(a) and 4(d)). This discrepancy arises because microwave absorption performance depends not only on inherent loss capability but also correlates with impedance matching. Impedance matching concerns the difference in characteristic impedance between free space and EM absorption materials [62]. When the characteristic impedance of an EM absorption materials does not align with that of free space, EM waves primarily reflect at the interface instead of penetrating the material. Thus, despite strong absorption capabilities, EM absorption materials with impedance mismatch cannot demonstrate effective EM absorption performance. Recent studies have frequently utilized the delta function (Δ) to quantify the degree of impedance matching, which can be calculated using Eqs. (6)–(8) [16]

$$|\Delta| = \left|\sinh^2(Kfd) - M\right| \quad (6)$$

$$K = \frac{4\pi\sqrt{\mu_r'\varepsilon_r'}\sin\frac{\delta_e + \delta_m}{2}}{c\cos\delta_e\cos\delta_m} \quad (7)$$

$$M = \frac{4\mu_r'\cos\delta_e\varepsilon_r'\cos\delta_m}{(\mu_r'\cos\delta_e - \varepsilon_r'\cos\delta_m)^2 + \left[\tan\left(\frac{\delta_m}{2} - \frac{\delta_e}{2}\right)\right]^2(\mu_r'\cos\delta_e + \varepsilon_r'\cos\delta_m)^2} \quad (8)$$

According to Eqs. (6)–(8), impedance matching maps were computed for Mo/DA-0.5, Mo/DA-1.0, and Mo/DA-1.5. As shown in Figs. 5(g)–5(i), $|\Delta|$ values close to 0 are considered perfect impedance matching, while $|\Delta| < 0.4$ is deemed acceptable impedance matching [22, 63]. Mo/DA-0.5 exhibits an area where $|\Delta| < 0.4$ covers approximately 33.5% (Fig. 5(g)). It is observed that with an increase in Mo_2C nanoparticles, Mo/DA-1.0 shows a significant increase in the area where $|\Delta| < 0.4$, suggesting potentially meritorious EM absorption performance (Fig. 5(h)).

With the introduction of more Mo_2C nanoparticles (Fig. 5(i)), Mo/DA-1.5 demonstrates attenuated impedance matching (coverage area where $|\Delta| < 0.4$ is 16.6%). From these results, it can be concluded that the superior microwave absorption performance of Mo/DA-1.0 is attributed to its good impedance matching and dielectric loss capabilities. Based on the above analysis, we attempt to elucidate the reason for the excellent microwave absorption performance of Mo_2C/C in Fig. 6(a). (1) The air trapped inside the constructed hollow structure brings the inherent impedance of the composite material closer to that of air, optimizing impedance matching. (2) The introduction of Mo_2C adjusts the dielectric properties of the composites, while the heterogeneous hollow structure facilitates the formation of a conductive network within the matrix, leading to significant conductivity loss. (3) The interlaced lamellar structure on the surface of the composite material and the internal cavities facilitates the scattering and reflection of incident EM wave, enhancing the multiple attenuation characteristics of EM wave. (4) The incorporation of Mo_2C nanoparticles into the carbon matrix creates abundant heterogeneous interfaces, causing uneven accumulation of free charges at these interfaces and increasing interface polarization loss. Additionally, the residual functional groups or defect sites of the carbon matrix and Mo_2C nanoparticles in Mo_2C/C can act as active sites for dipole orientation polarization under alternating EM fields, enhancing the dipole polarization loss effect.

Radar cross-section (RCS) is a crucial parameter reflecting the EM absorption capability of an aircraft under real far-field conditions. In spherical coordinates, θ and φ determine the scattering direction, and the RCS value can be calculated using the following Eq. (9) [63–65]

$$\sigma = 10\log\left(\frac{4\pi S}{\lambda^2}\left|\frac{E_s}{E_i}\right|\right)^2 \quad (9)$$

where S, E_s, and E_i are the simulated plate, electric field intensity of transmitting waves and receiving waves, respectively. The 3D RCS maps for perfect electric conductor (PEC) and Mo_2C/C coatings on PEC are shown in Figs. 6(b)–6(f). The results indicate that the scattering signal is strongest across the entire detection angle range for the pure PEC substrate. However, when the surface is coated with the Mo_2C/C composites, the scattering signal notably decreases. Detailed RCS values for PEC and Mo_2C/C within −60° < θ < 60° are shown in Fig. 6(d). The maximum RCS value for PEC approaches 20 dBm² at 0°. After coating with the Mo_2C/C composites, the RCS values of all three samples are reduced compared to pure PEC, with Mo/DA-1.0 exhibiting the most significant reduction. Specifically, the maximum RCS value for Mo/DA-1.0 is only 3.8 dBm². These results underscore the significant potential of Mo/DA-1.0 in developing radar stealth coatings and its practical applicability under real far-field conditions.

4 Conclusions

In summary, a hierarchical hollow microsphere composed of carbon nanosheets decorated with Mo_2C nanoparticles was synthesized through converting the precursor obtained by coupling dopamine hydrochloride and ammonium molybdate under high temperature. The molar ratio of dopamine hydrochloride not only plays a crucial role in the creation of hollow structure, but also affords the effect of compositional regulation. The results indicate that combining components with hollow structure is an efficient method for optimizing EM properties and achieving strong EM energy attenuation. Especially for the composite with the content of Mo_2C nanoparticles at 43.2%, the reflection loss intensity and the maximum effective absorption bandwidth can reach −70.2 dB and 6.2 GHz, respectively. The mechanism investigation reveals that conductivity loss, polarization loss, and hollow structure, are together responsible for powerful attenuation ability. Radar cross-section simulation calculations further demonstrate that the Mo_2C/C composites exhibit remarkable characteristics for far-field applications, indicating broad application prospects in EM absorption.

Electronic Supplementary Material: Supplementary material (the XPS spectra of Mo_2C/C composites; the real (a) and imaginary (b) parts of relative complex permeability of Mo_2C/C composites; the Cole–Cole circles of Mo/DA-0.5 (a), Mo/DA-1.0 (b), and Mo/DA-1.5 (c)) is available in the online version of this article at https://doi.org/10.26599/NR.2025.94907034.

Data availability

All data needed to support the conclusions in the paper are presented in the manuscript and the Electronic Supplementary

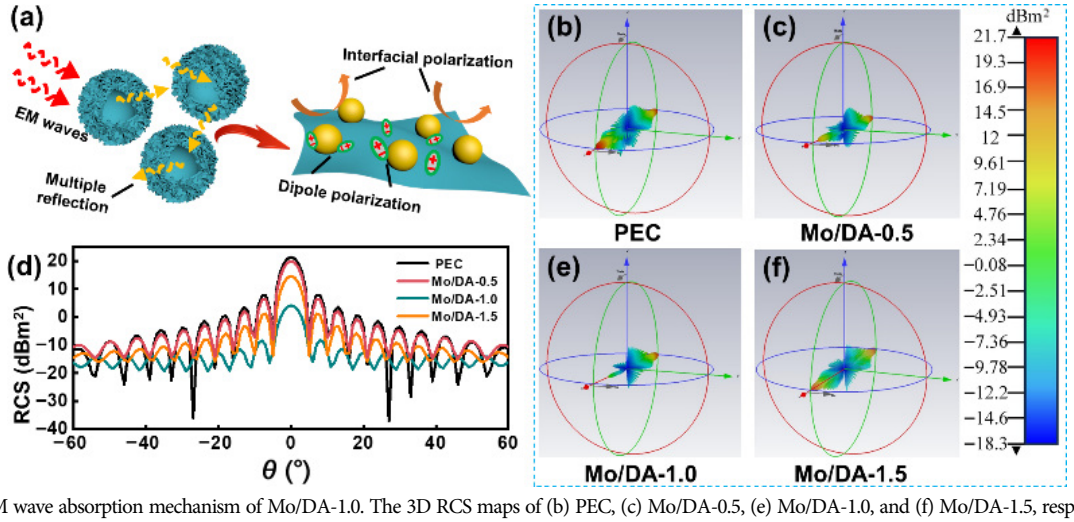

Figure 6 (a) EM wave absorption mechanism of Mo/DA-1.0. The 3D RCS maps of (b) PEC, (c) Mo/DA-0.5, (e) Mo/DA-1.0, and (f) Mo/DA-1.5, respectively. (d) RCS simulated curves of PEC and Mo_2C/C composites.

Material. Additional data related to this paper may be requested from the corresponding author upon request.

Acknowledgements

This work is supported by the National University of Defense Technology Independent Innovation Science Fund (No. 24-ZZCX-JDZ-42) and the Postdoctoral Fellowship Program of CPSF (No. GZC20241747).

Declaration of competing interest

All the contributing authors report no conflict of interests in this work.

Author contribution statement

Z. S. C.: Data curation, project administration, writing manuscript. Y. H. W.: Data curation, project administration, validation, experimental design, funding acquisition. Y. L.: Project administration, writing manuscript. Z. G. L.: Project administration, data curation. X. Y. L.: Writing manuscript, validation. L. P. L.: Data curation, writing manuscript. Y. J. C.: Project administration, writing manuscript. J. M. S.: Project administration, experimental design. X. Z.: Data curation, funding acquisition, validation. All the authors have approved the final manuscript.

Use of AI statement

None.

References

[1] Gai, L. X.; Wang, Y. H.; Wan, P.; Yu, S. P.; Chen, Y. Z.; Han, X. J.; Xu, P.; Du, Y. C. Compositional and hollow engineering of silicon carbide/carbon microspheres as high-performance microwave absorbing materials with good environmental tolerance. *Nano-Micro Lett.* **2024**, *16*, 167.

[2] Zhu, J. H.; Lan, D.; Liu, X. H.; Zhang, S. H.; Jia, Z. R.; Wu, G. L. Porous structure fibers based on multi-element heterogeneous components for optimized electromagnetic wave absorption and self-anticorrosion performance. *Small*, in press, https://doi.org/10.1002/smll.202403689.

[3] Jia, Z. R.; Sun, L. F.; Gao, Z. G.; Lan, D. Modulating magnetic interface layer on porous carbon heterostructures for efficient microwave absorption. *Nano Res.* **2024**, *18*, 10099–10108.

[4] Calvo-de La Rosa, J.; Bou-Comas, A.; Hernàndez, J. M.; Marín, P.; Lopez-Villegas, J. M.; Tejada, J.; Chudnovsky, E. M. New approach to designing functional materials for stealth technology: Radar experiment with bilayer absorbers and optimization of the reflection loss. *Adv. Funct. Mater.* **2024**, *34*, 2308819.

[5] Liu, Y. L.; Zhang, M. H.; Liu, D. W.; Gai, L. X.; Wang, Y.; Wang, P.; Han, X. J.; Du, Y. C. A self-foaming strategy to construct small Mo_2C nanoparticles decorated 3D carbon foams as superior electromagnetic wave absorbing materials with strong corrosion resistance. *Small Methods*, in press, https://doi.org/10.1002/smtd.202400734.

[6] Wang, Y.; Cheng, R. R.; Cui, W. G.; Lu, Z.; Yang, Y. X.; Pan, H. G.; Che, R. C. Heterostructure design of 3D hydrangea-like Fe_3O_4/Fe_7S_8@C core–shell composite as a high-efficiency microwave absorber. *Carbon* **2023**, *210*, 118043.

[7] Luo, J. H.; Li, X. P.; Yan, W. X.; Shu, P. C.; Mei, J. RGO supported bimetallic MOFs-derived Co/MnO/porous carbon composite toward broadband electromagnetic wave absorption. *Carbon* **2023**, *205*, 552–561.

[8] Yu, Y. D.; Fang, Y.; Hu, Q.; Shang, X. N.; Tang, C. C.; Meng, F. B. Hollow MOF-derived CoNi/C composites as effective electromagnetic absorbers in the X-band and Ku-band. *J. Mater. Chem. C* **2022**, *10*, 983–993.

[9] Pan, F.; Liu, Z. C.; Deng, B. W.; Dong, Y. Y.; Zhu, X. J.; Huang, C.; Lu, W. Lotus leaf-derived gradient hierarchical porous C/MoS_2 morphology genetic composites with wideband and tunable electromagnetic absorption performance. *Nano-Micro Lett.* **2021**, *13*, 43.

[10] Su, Q.; He, Y. F.; Liu, D. D.; Li, D. G.; Xia, L.; Huang, X. X.; Zhong, B. Facile fabrication of graphene/g-C_3N_4 for electromagnetic wave absorption. *Nano Res.* **2024**, *17*, 1687–1698.

[11] Yang, X.; Xuan, L. X.; Men, W. W.; Wu, X.; Lan, D.; Shi, Y. P.; Jia, H. X.; Duan, Y. P. Carbonyl iron/glass fiber cloth composites: Achieving multi-spectrum stealth in a wide temperature range. *Chem. Eng. J.* **2024**, *491*, 151862.

[12] Dai, S. S.; Cheng, Y.; Quan, B.; Liang, X. H.; Liu, W.; Yang, Z. H.; Ji, G. B.; Du, Y. W. Porous-carbon-based Mo_2C nanocomposites as excellent microwave absorber: A new exploration. *Nanoscale* **2018**, *10*, 6945–6953.

[13] Yang, K.; Cui, Y. H.; Wan, L. Y.; Wang, Y. B.; Tariq, M. R.; Liu, P.; Zhang, Q. Y.; Zhang, B. L. Preparation of three-dimensional Mo_2C/NC@MXene and its efficient electromagnetic absorption properties. *ACS Appl. Mater. Interfaces* **2022**, *14*, 7109–7120.

[14] Wang, Y. H.; Li, C. L.; Han, X. J.; Liu, D. W.; Zhao, H. H.; Li, Z. N.; Xu, P.; Du, Y. C. Ultrasmall Mo_2C nanoparticle-decorated carbon polyhedrons for enhanced microwave absorption. *ACS Appl. Nano Mater.* **2018**, *1*, 5366–5376.

[15] Wang, Y. H.; Han, X. J.; Xu, P.; Liu, D. W.; Cui, L. R.; Zhao, H. H.; Du, Y. C. Synthesis of pomegranate-like Mo_2C@C nanospheres for highly efficient microwave absorption. *Chem. Eng. J.* **2019**, *372*, 312–320.

[16] Wang, Y. H.; Zhang, M. H.; Deng, X. S.; Li, Z. G.; Chen, Z. S.; Shi, J. M.; Han, X. J.; Du, Y. C. Reduced graphene oxide aerogel decorated with Mo_2C nanoparticles toward multifunctional properties of hydrophobicity, thermal insulation and microwave absorption. *Int. J. Miner. Metall. Mater.* **2023**, *30*, 536–547.

[17] Tan, D. L.; Wang, Q.; Li, M. R.; Song, L. M.; Zhang, F.; Min, Z. Y.; Wang, H. L.; Zhu, Y. Q.; Zhang, R.; Lan, D. et al. Magnetic media synergistic carbon fiber@Ni/NiO composites for high-efficiency electromagnetic wave absorption. *Chem. Eng. J.* **2024**, *492*, 152245.

[18] Lan, D.; Hu, Y.; Wang, M.; Wang, Y.; Gao, Z. G.; Jia, Z. R. Perspective of electromagnetic wave absorbing materials with continuously tunable effective absorption frequency bands. *Compos. Commun.* **2024**, *50*, 101993.

[19] Wu, Z. C.; Cheng, H. W.; Jin, C.; Yang, B. T.; Xu, C. Y.; Pei, K.; Zhang, H. B.; Yang, Z. Q.; Che, R. C. Dimensional design and core-shell engineering of nanomaterials for electromagnetic wave absorption. *Adv. Mater.* **2022**, *34*, 2107538.

[20] Huang, W. H.; Zhang, X. X.; Zhao, Y. N.; Zhang, J.; Liu, P. B. Hollow N-doped carbon polyhedra embedded Co and Mo_2C nanoparticles for high-efficiency and wideband microwave absorption. *Carbon* **2020**, *167*, 19–30.

[21] Zhao, T. B.; Jia, Z. R.; Zhang, Y.; Wu, G. L. Multiphase molybdenum carbide doped carbon hollow sphere engineering: The superiority of unique double-shell structure in microwave absorption. *Small* **2023**, *19*, 2206323.

[22] Deng, X. S.; Wang, Y. H.; Ma, L. F.; Li, Z. G.; Chen, Z. S.; Lv, X. Y.; Chang, Y. J.; Liu, Y.; Shi, J. M. Construction of dual-shell Mo_2C/C microsphere towards efficient electromagnetic wave absorption. *Int. J. Mol. Sci.* **2022**, *23*, 14502.

[23] Diao, L. C.; Qin, J.; Zhao, N. Q.; Shi, C. S.; Liu, E. Z.; He, F.; Ma, L. Y.; Li, J. J.; He, C. N. "Ethanol-water exchange" nanobubbles templated hierarchical hollow β-Mo_2C/N-doped carbon composite nanospheres as an efficient hydrogen evolution electrocatalyst. *J. Mater. Chem. A* **2018**, *6*, 6054–6064.

[24] Wang, Y. H.; Li, X. D.; Han, X. J.; Xu, P.; Cui, L. R.; Zhao, H. H.; Liu, D. W.; Wang, F. Y.; Du, Y. C. Ternary Mo_2C/Co/C composites with enhanced electromagnetic waves absorption. *Chem. Eng. J.* **2020**, *387*, 124159.

[25] Qutaish, H.; Tanaka, S.; Kaneti, Y. V.; Lin, J. J.; Bando, Y.; Alshehri, A. A.; Yusa, S. I.; Yamauchi, Y.; Hossain, M. S. A.; Kim, J. Soft-templated synthesis of mesoporous nickel oxide using poly(styrene-*block*-acrylic acid-*block*-ethylene glycol) block copolymers. *Microporous Mesoporous Mater.* **2018**, *271*, 16–22.

[26] He, Z. Z.; Sun, R.; Xu, H. X.; Geng, W. C.; Liu, P. B. Metal-organic-frameworks derived hollow carbon derivatives: Controllable configurations and optimized microwave absorption. *Carbon* **2024**, *219*, 118853.

[27] Ma, G. J.; Lan, D.; Zhang, Y.; Sun, X. Y.; Jia, Z. R.; Wu, G. L.; Bu, G. X.; Yin, P. F. Microporous cobalt ferrite with bio-carbon loosely decorated to construct multi-functional composite for dye adsorption, anti-bacteria and electromagnetic protection. *Small*, in press, https://doi.org/10.1002/smll.202404449.

[28] Yu, S. P.; Gai, L. X.; Tian, C. H.; Zhu, L.; Song, W. K.; Hu, B.; Han, X. J.; Du, Y. C. Multi-interface spatial star-like MoC/Co/C composites toward enhanced electromagnetic wave absorption properties. *Carbon* **2024**, *228*, 119390.

[29] Liu, Y. L.; Wang, F. Y.; Wang, Y. H.; Hu, B.; Xu, P.; Han, X. J.; Du, Y. C. A combined engineering of hollow and core–shell structures for C@MoS_2 microcapsules toward high-efficiency electromagnetic absorption. *Compos. Part B: Eng.* **2024**, *273*, 111244.

[30] Chen, X. T.; Wu, Y.; Gu, W. H.; Zhou, M.; Tang, S. L.; Cao, J. M.; Zou, Z. Q.; Ji, G. B. Research progress on nanostructure design and composition regulation of carbon spheres for the microwave absorption. *Carbon* **2022**, *189*, 617–633.

[31] Wang, N.; Ma, W. J.; Ren, Z. Q.; Du, Y. C.; Xu, P.; Han, X. J. Prussian blue analogues derived porous nitrogen-doped carbon microspheres as high-performance metal-free peroxymonosulfate activators for non-radical-dominated degradation of organic pollutants. *J. Mater. Chem. A* **2018**, *6*, 884–895.

[32] Chen, X. L.; Lan, D.; Zhou, L. T.; Zeng, Z.; Liu, Y. K.; Du, S. X.; Zou, Z. Y.; Wu, G. L. Rational construction of $ZnFe_2O_4$ decorated hollow carbon cloth towards effective electromagnetic wave absorption. *Ceram. Int.* **2024**, *50*, 24549–24557.

[33] Ferrari, A. C.; Robertson, J. Interpretation of Raman spectra of disordered and amorphous carbon. *Phys. Rev. B* **2000**, *61*, 14095–14107.

[34] Zhang, Q. C.; Du, Z. J.; Hou, M. M.; Ding, Z. Z.; Huang, X. Z.; Chen, A. L.; Ma, Y. T.; Lu, S. J.; Tang, X. Z. Ultralight, anisotropic, and self-supported graphene/MWCNT aerogel with high-performance microwave absorption. *Carbon* **2022**, *188*, 442–452.

[35] Wu, C.; Chen, Z. F.; Wang, M. L.; Cao, X.; Zhang, Y.; Song, P.; Zhang, T. Y.; Ye, X. L.; Yang, Y.; Gu, W. H. et al. Confining tiny MoO_2 clusters into reduced graphene oxide for highly efficient low frequency microwave absorption. *Small* **2020**, *16*, 2001686.

[36] Zhao, T. B.; Lan, D.; Jia, Z. R.; Gao, Z. G.; Wu, G. L. Hierarchical porous molybdenum carbide synergic morphological engineering towards broad multi-band tunable microwave absorption. *Nano Res.* **2024**, *18*, 9845–9856.

[37] Yang, P.; Zhao, H. X.; Yang, Y. N.; Zhao, P. X.; Zhao, X. C.; Yang, L. J. Fabrication of N, P-codoped Mo_2C/carbon nanofibers via electrospinning as electrocatalyst for hydrogen evolution reaction. *ES Mater. Manuf.* **2020**, *7*, 34–39.

[38] Yang, C.; Guo, K. K.; Yuan, D. W.; Cheng, J. L.; Wang, B. Unraveling reaction mechanisms of Mo_2C as cathode catalyst in a Li-CO_2 battery. *J. Am. Chem. Soc.* **2020**, *142*, 6983–6990.

[39] Zhou, Q. P.; Zhang, X. C.; Wu, Y. C.; Jiang, X. Y.; Li, T. S.; Chen, M.; Ni, L. B.; Diao, G. W. Polyoxometalates@metal-organic frameworks derived bimetallic Co/Mo_2C nanoparticles embedded in carbon nanotube-interwoven hierarchically porous carbon polyhedron composite as a high-efficiency electrocatalyst for Al-S batteries. *Small* **2023**, *19*, 2304515.

[40] Zhang, Z. J.; Zhao, J.; Wu, M. C.; Lu, Q. H.; Liu, R. Three-phase interface induced charge modulation on MoO_2/Mo_2C-carbon tube for enhanced hydrogen evolution. *Nano Res.* **2023**, *16*, 4706–4714.

[41] Zhang, D. T.; Liu, M. C.; Li, J.; Zhang, Y. S.; Zhang, B. M.; Lu, C.; Hu, Y. X.; Wu, K. P.; Kong, L. B. Design of kinetic well-matched Mo_2C nanoparticles anchored into 3D hierarchical porous carbon towards high-rate sodium ion storage. *Electrochim. Acta* **2021**, *372*, 137860.

[42] Cao, X. L.; Liu, X. H.; Zhu, J. H.; Jia, Z. R.; Liu, J. K.; Wu, G. L. Optimal particle distribution induced interfacial polarization in hollow double-shell composites for electromagnetic waves absorption performance. *J. Colloid Interface Sci.* **2023**, *634*, 268–278.

[43] Zhou, P. P.; Zhang, S. Y.; Zhou, W.; Sun, C. C.; Hu, C. Y.; Yuan, S. L.; Li, J. R.; Liu, C.; Zhao, Y. C.; Kuang, Y. W. et al. Hollow engineering of Co/N-doped C@carbon aerogel with hierarchical structure boosting interfacial polarization for ultra-thin microwave absorption and thermal insulation. *Chem. Eng. J.* **2024**, *495*, 153561.

[44] Li, Z. J.; Zhang, L. M.; Wu, H. J. A regulable polyporous graphite/melamine foam for heat conduction, sound absorption and electromagnetic wave absorption. *Small* **2024**, *20*, 2305120.

[45] Wu, Z.; Tan, X. L.; Wang, J. Q.; Xing, Y. Q.; Huang, P.; Li, B. J.; Liu, L. MXene hollow spheres supported by a C-Co exoskeleton grow MWCNTs for efficient microwave absorption. *Nano-Micro Lett.* **2024**, *16*, 107.

[46] Li, J. J.; Lan, D.; Cheng, Y. H.; Jia, Z. R.; Liu, P. B.; Shi, X. T.; Guo, H.; Feng, A. L.; Feng, X.; Wu, G. L. et al. Constructing mixed-dimensional lightweight magnetic cobalt-based composites heterostructures: An effective strategy to achieve boosted microwave absorption and self-anticorrosion. *J. Mater. Sci. Technol.* **2024**, *196*, 60–70.

[47] Ling, A.; Tan, G. G.; Man, Q. K.; Lou, Y. X.; Chen, S. W.; Gu, X. S.; Li, R. W.; Pan, J.; Liu, X. C. Broadband microwave absorbing materials based on MWCNTs' electromagnetic wave filtering effect. *Compos. Part B: Eng.* **2019**, *171*, 214–221.

[48] Fu, M.; Yu, H.; Chen, W. Construction of Co_3O_4 porous rod/graphene heterostructures toward strong and broadband microwave absorption applications. *Appl. Surf. Sci.* **2023**, *622*, 156946.

[49] Zhao, H. H.; Xu, X. Z.; Wang, Y. H.; Fan, D. G.; Liu, D. W.; Lin, K. F.; Xu, P.; Han, X. J.; Du, Y. C. Heterogeneous interface induced the formation of hierarchically hollow carbon microcubes against electromagnetic pollution. *Small* **2020**, *16*, 2003407.

[50] Chen, G.; Liang, H. S.; Yun, J. J.; Zhang, L. M.; Wu, H. J.; Wang, J. Y. Ultrasonic field induces better crystallinity and abundant defects at grain boundaries to develop CuS electromagnetic wave absorber. *Adv. Mater.* **2023**, *35*, 2305586.

[51] Wang, Y.; Qu, Z. J.; Wang, W.; Qian, H. F.; Song, X. Y.; Yu, D. Multidimensional nanomaterials synergistic polyimide nanofiber/MXene/$NiFe_2O_4$ hybrid aerogel for high-performance microwave absorption. *Chem. Eng. J.* **2023**, *470*, 144435.

[52] Wang, F. Y.; Liu, Y. L.; Feng, R. D.; Wang, X.; Han, X. J.; Du, Y. C. A "win–win" strategy to modify Co/C foam with carbon microspheres for enhanced dielectric loss and microwave absorption characteristics. *Small* **2023**, *19*, 2303597.

[53] Zeng, X. J.; Ning, Y.; Guo, H. H.; Xie, N. H.; Yu, R. H. Dual template induced assembly of 2D nanosheets to 3D porous Mo_2C/NiFe-NC networkers for electromagnetic wave absorption. *Mater. Today Phys.* **2023**, *34*, 101077.

[54] Wen, B.; Yang, G. R.; Wang, Y. F.; Liu, X. F.; Weng, X. J.; Jing, D. W.; Ding, S. J. *In situ* derived porous CoNi@Mo_2C-CNT composites for excellent electromagnetic wave absorption properties. *Cryst. Growth Des.* **2022**, *22*, 7339–7348.

[55] Chen, L.; Sui, J.; Waterhouse, G. I. N.; Zhang, Z. M.; Yu, L. M. $Fe_{0.64}Ni_{0.36}$@C and Mo_2C@C heterostructures embedded in N-doped carbons as microwave absorbers. *J. Alloys Compd.* **2023**, *960*, 170820.

[56] Wen, J. M.; Chen, G.; Hui, S. C.; Li, Z. J.; Yun, J. J.; Fan, X. M.; Zhang, L. M.; He, Q.; Liu, X. M.; Wu, H. J. Plasma induced dynamic coupling of microscopic factors to collaboratively promote EM losses coupling of transition metal dichalcogenide absorbers. *Adv. Powder Mater.* **2024**, *3*, 100180.

[57] Chen, X. L.; Zhang, F.; Lan, D.; Zhang, S. J.; Du, S. X.; Zhao, Z. W.; Ji, G. B.; Wu, G. L. State-of-the-art synthesis strategy for nitrogen-doped carbon-based electromagnetic wave absorbers: From the perspective of nitrogen source. *Adv. Compos. Hybrid Mater.* **2023**, *6*, 220.

[58] Wu, Y.; Chen, L.; Han, Y. X.; Liu, P. B.; Xu, H. H.; Yu, G. Z.; Wang, Y. Y.; Wen, T.; Ju, W. B.; Gu, J. W. Hierarchical construction of CNT networks in aramid papers for high-efficiency microwave absorption. *Nano Res.* **2023**, *16*, 7801–7809.

[59] Chen, G.; Li, Z. J.; Zhang, L. M.; Chang, Q.; Chen, X. J.; Fan, X. M.; Chen, Q.; Wu, H. J. Mechanisms, design, and fabrication strategies for emerging electromagnetic wave-absorbing materials. *Cell Rep. Phys. Sci.* **2024**, *5*, 102097.

[60] Zhao, J.; Gu, Z.; Zhang, Q. G. Stacking MoS_2 flower-like microspheres on pomelo peels-derived porous carbon nanosheets for high-efficient X-band electromagnetic wave absorption. *Nano Res.* **2024**, *17*, 1607–1615.

[61] Li, X. A.; Jin, K. X.; Qu, X. Y.; Shi, Y. N.; Wang, C. S.; Guo, W. C.; Tian, K. S.; Wang, Y. H.; Wang, H. Y. Magnetic bimetallic nanoparticles confined growth for enhancement of electromagnetic loss in void@Fe@SiO2/Co/C particles. *Chem. Eng. J.* **2024**, *498*, 155786.

[62] He, Y. F.; Su, Q.; Liu, D. D.; Xia, L.; Huang, X. X.; Lan, D.; Liu, Y. A.; Huang, Y. D.; Zhong, B. Surface engineering strategy for MXene to tailor electromagnetic wave absorption performance. *Chem. Eng. J.* **2024**, *491*, 152041.

[63] Wang, Y. C.; Yao, L. H.; Zheng, Q.; Cao, M. S. Graphene-wrapped multiloculated nickel ferrite: A highly efficient electromagnetic attenuation material for microwave absorbing and green shielding. *Nano Res.* **2022**, *15*, 6751–6760.

[64] Gao, Z. G.; Lan, D.; Ren, X. Y.; Jia, Z. R.; Wu, G. L. Manipulating cellulose-based dual-network coordination for enhanced electromagnetic wave absorption in magnetic porous carbon nanocomposites. *Compos. Commun.* **2024**, *48*, 101922.

[65] Gai, L. X.; Zhao, H. H.; Wang, F. Y.; Wang, P.; Liu, Y. L.; Han, X. J.; Du, Y. C. Advances in core-shell engineering of carbon-based composites for electromagnetic wave absorption. *Nano Res.* **2022**, *15*, 9410–9439.